Biomaterials Science

ROYAL SOCIETY OF CHEMISTRY

PAPER

View Article Online
View Journal | View Issue

Cite this: *Biomater. Sci.*, 2024, **12**, 6403

Redox nanodrugs alleviate chronic kidney disease by reducing inflammation and regulating ROS†

Qin Wang,*‡[a] Xuedan Nie,‡[b] Yifan Song,[a] Haiyan Qiu,[c] Liting Chen,[a] He Zhu,[a] Xueli Zhang,[a] Mengru Yang,[a] Xiaohui Xu,[a] Peidan Chen,[a] Chao Zhang,[a] Jia Xu,[a] Yeping Ren*[a] and Wenting Shang *[c]

Immune-mediated glomerular diseases lead to chronic kidney disease (CKD), primarily through mechanisms such as immune cell overactivation, mitochondrial dysfunction and imbalance of reactive oxygen species (ROS). We have developed an ultra-small nanodrug composed of Mn_3O_4 nanoparticles which is functionalized with biocompatible ligand citrate (C-Mn_3O_4 NPs) to maintain cellular redox balance in an animal model of oxidative injury. Furthermore, this ultra-small nanodrug, loaded with tacrolimus (Tac), regulated the activity of immune cells. We established a doxorubicin (DOX)-induced CKD model in SD rats using conditions of oxidative distress. The results demonstrate the ROS scavenging capability of Mn_3O_4 NPs, which mimics enzymatic activity, and the immunosuppressive effect of tacrolimus. This combination promotes targeted accumulation in the renal region with sustained drug release through the enhanced permeability and retention (EPR) effect. Tac@C-Mn_3O_4 protects the structural and functional integrity of mitochondria from oxidative damage while eliminating excess ROS to maintain cellular redox homeostasis, thereby suppressing the overexpression of pro-inflammatory cytokines to restore kidney function and preserve a normal kidney structure, reducing inflammation and regulating antioxidant stress pathways. This dual-pronged treatment strategy also provides novel strategies for CKD management and demonstrates substantial potential for clinical translational application.

Received 3rd July 2024,
Accepted 19th October 2024

DOI: 10.1039/d4bm00881b

rsc.li/biomaterials-science

Introduction

Chronic kidney disease (CKD) is a highly prevalent condition, affecting 8% to 16% of the global population.[1] There is a steady increase in its morbidity and mortality rates. This pose a significant burden on society health resources. CKD is characterized by a persistent and irreversible reduction in nephron number, leading to glomerulosclerosis, tubulointerstitial fibrosis, and arteriosclerosis, and this ultimately leads to life-threatening renal failure.[2,3] The kidneys contain over a million nephrons. Conventional treatments face significant challenges in achieving organ-specific or cell-specific delivery following renal damage. Furthermore, achieving therapeutic effects typically requires higher dosage, which can lead to serious adverse reactions.[4–6] Therefore, a more specific drug delivery system targeting the kidney is a key and emerging development trend in the treatment of CKD.

Mitochondria produce reactive oxygen species (ROS) during cellular respiration through the electron transport chain (ETC) and cell signaling pathways. Complexes I and III produce superoxide anions ($^{\bullet}O^{2-}$) and hydrogen peroxide (H_2O_2). Mitochondria are also involved in cell signaling, such as the production of ROS by NADPH oxidase (NOX) and cytochrome P450 enzymes.[7] Excess production of ROS serves as a secondary messenger in cell signaling, influencing processes such as metabolic cell survival and death.[8] Excessive ROS accumulation is implicated in the pathogenesis of CKD, leading to severe constriction and structural remodelling of glomerular arteries, characterized by thickening of the vessel wall and narrowing of the lumen.[9,10] The persistently high levels of oxidative stress can severely disrupt the cellular structure and function, inducing cell death.[11] Therefore, maintaining the homeostasis between ROS production and clearance through multiple mechanisms is crucial, which is also the key to developing ROS-targeted therapies for CKD.

Recent studies have investigated various natural or synthetic antioxidants such as α-tocopherol, ascorbic acid, β-carotene, curcumin, *etc.* for their ability to scavenge over-

[a]*Department of Nephrology, Shenzhen University General Hospital, Shenzhen University, Shenzhen, Guangdong, 518000, China. E-mail: wangqinmail@vip.163.com, renyeping123@126.com*
[b]*Department of Neurology, South China Hospital, Medical School, Shenzhen University, Shenzhen, Guangdong, 518116, China*
[c]*CAS Key Laboratory of Molecular Imaging, Institute of Automation, Chinese Academy of Sciences, Beijing, 100190, China. E-mail: wenting.shang@ia.ac.cn*

†Electronic supplementary information (ESI) available. See DOI: https://doi.org/10.1039/d4bm00881b

‡These authors contributed equally to this work.

expressed intracellular ROS and combat oxidative stress in the treatment of various inflammatory diseases.[12,13] Although these compounds show promise in reducing ROS levels, many traditional antioxidant molecules are unable to selectively target oxidation products or free radicals that serve as important physiological signaling messengers.[14] Moreover, meta-analyses of clinical trials indicate that traditional antioxidants can, to some extent, accelerate the onset of death.[8,15] In contrast, antioxidant nanosystems have demonstrated significant advantages including broad-spectrum ROS scavenging activity, satisfactory biocompatibility and biosafety,[16] making substantial progress in treating kidney diseases.[17,18] For example, targeted nanodrug delivery systems designed to reach specific renal cells, such as glomerular endothelial cells, the glomerular basement membrane, and mesangial cells, have successfully optimized drug levels and therapeutic effects while minimizing toxic side effects by modifying nanoparticle surface properties.[19] As reported in the literature, the novel superoxide dismutase/catalase mimetic materials, Tempol and phenylboronic acid pinacol ester conjugated β-cyclodextrin (TPCD), and inflammation-regulating microspheres can both mimic superoxide dismutase (SOD) to clear ROS and exhibit excellent therapeutic effects in acute kidney injury.[20,21] Zhang *et al.* designed Cu-SAzyme with high SOD activity, primarily mimicking the activity of SOD enzyme to remove $^{\bullet}O^{2-}$.[22] Wei *et al.* demonstrated that Mn_3O_4 nanoparticles (NPs) have a variety of enzymatic mimetic activities that eliminate $^{\bullet}O^{2-}$ by disproportionating $^{\bullet}O^{2-}$ into H_2O_2 and O_2 in the dual oxidation states of Mn^{2+} and Mn^{3+}.[23] In addition, Mn_3O_4 NPs can further catalyze the decomposition of H_2O_2 and the scavenging of $^{\bullet}OH$, outperforming CeO_2 NPs, and provide a promising strategy for the treatment of inflammation using redox activity nanozymes.

Although the application of nanopreparations as a carrier for targeted kidney delivery shows considerable promise, the stringent requirements related to particle size, charge, shape, hydrophilicity and rigid structure of the renal filtration barrier pose significant challenges.[17] As an immunosuppressant, tacrolimus (Tac) reduces the immune response and inflammatory damage in the kidneys by inhibiting T lymphocyte activation and function.[24] However, in clinical settings, high doses of Tac can induce nephrotoxicity and other adverse effects, exacerbating CKD progression. Additionally, there are significant variations in the metabolic capacity of Tac, necessitating more individualized dose adjustment and posing further challenge to clinical application.

To address these issues, an ultra-small nanopreparation, Tac@C-Mn_3O_4, was developed using citric acid-coated Mn_3O_4 NPs loaded with Tac drugs. These nanoparticles accumulate in the lesion area and achieve sustained drug release by targeting the inflammatory microenvironment under the EPR effect. This approach has a superior therapeutic effect in treating proteinuria and renal fibrosis caused by CKD through reducing inflammation and regulating the antioxidant stress pathway. The redox ultra-small nanopreparation provided by this study represents a new dual-strategy for treating CKD through anti-inflammatory and antioxidant stress pathways, demonstrating great potential in clinical treatment (Scheme 1).

Methods

Materials

Tacrolimus was purchased from APExBIO (USA), $MnCl_2$ was obtained from Aladdin, while other reagents were purchased from Innochem. A CCK8 assay kit was purchased from Abbkine, and Calcein-AM dye and PI dye were purchased from Biosharp. DCFH-DA was acquired from Meilunbio Company (Dalian, China). An ELISA kit was provided by Boyan Biotech (China). Cells were purchased from Mlbio Company (Shanghai, China). JC-1 was purchased from Beyotime.

Synthesis of nanopreparations

The synthesis sequence for Mn_3O_4, C-Mn_3O_4, Tac@C-Mn_3O_4 and C-Mn_3O_4/ICG involved first dissolving 0.598 g $MnCl_2$ solution in 30 mL ethanolamine solution and sonication until a clear brown solution was obtained. An equal volume of deionized water was added, stirred at room temperature for 6 h, and centrifuged at 3000 rpm for 15 min using a centrifuge (H1750R, China). The resulting black pellet was washed three times with absolute ethanol to remove excess ethanolamine and dried at 60 °C to produce shiny black Mn_3O_4 nanoparticles. These nanoparticles were then added to 0.5 M citric acid (pH = 7.0) solution (150 mg Mn_3O_4 corresponding to 6 mL citric acid solution), and mixed in a mixer for 10 h. The large unfunctionalized particles were filtered out with a 0.22 μm filter, and the resultant C-Mn_3O_4 filtrate was used for the subsequent experiment. Tacrolimus, dissolved in chloroform, was mixed with this solution at a mass ratio of 1 : 1 and stirred overnight until the chloroform completely evaporated. The final product, Tac@C-Mn_3O_4 was then centrifuged to separate any unloaded Tac pellets. ICG was dissolved in DMSO solvent (1 mg mL^{-1}), and the same volume of C-Mn_3O_4 was added, the mixture was stirred for 3 h, and then a 500-Da dialysis bag was used to dialyse the mixture for 48 h to remove the free dye to obtain C-Mn_3O_4/ICG.

Performance testing

Morphology was observed using transmission electron microscopy (TEM, Talos F200x FEI, USA). Absorption spectra of Mn_3O_4, C-Mn_3O_4, Tac@C-Mn_3O_4 and C-Mn_3O_4/ICG solutions at a concentration of 0.1 mg mL^{-1} were obtained using a UV-2600 spectrophotometer (Shimadzu, Japan), covering a scanning band of 200–900 nm. The FT-IR spectra of Mn_3O_4, Tac, and Tac@C-Mn_3O_4 solutions were recorded using a Nicolet iS 10 spectrometer. The cumulative release of Tac from Tac@C-Mn_3O_4 at different times in PBS solutions with pH 5.5 and 7.4 was determined using a UV-2600 (Shimadzu). Serum stability of Tac@C-Mn_3O_4 and C-Mn_3O_4/ICG solutions was detected using a UV-2600 (Shimadzu). The particle size and zeta potential were determined using a BeNano 90 Zeta.

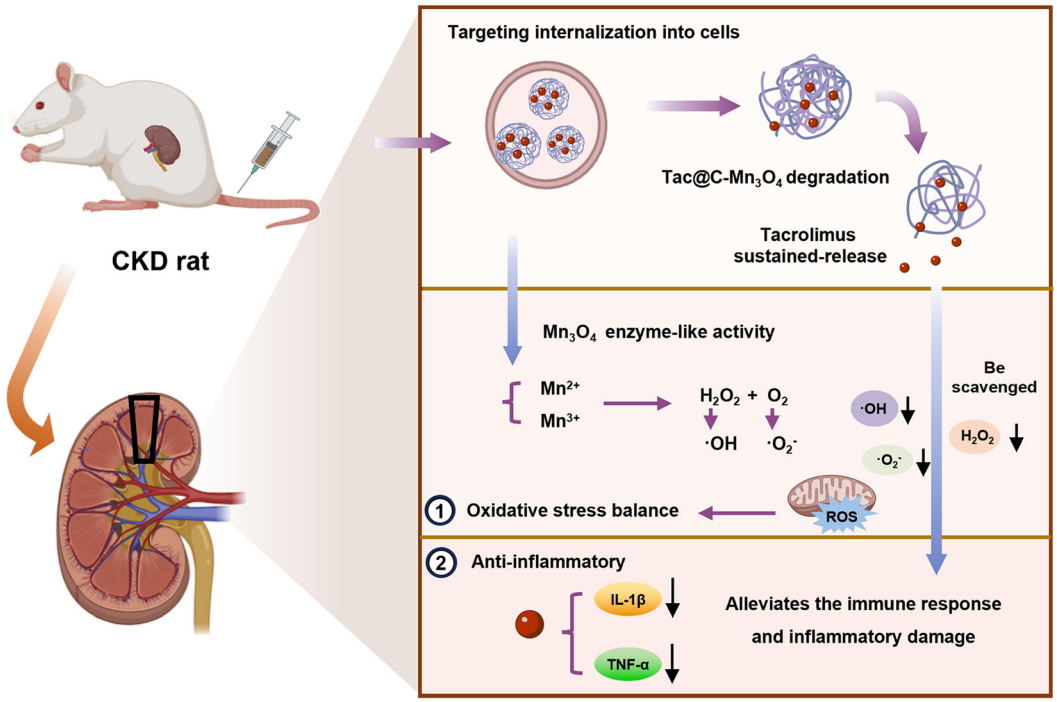

Scheme 1 Tac@C-Mn_3O_4 targeted the lesion area to enhance the efficacy of CKD treatment by regulating antioxidative stress pathways and reducing inflammation.

The encapsulation ratio and drug loading ratio were calculated according to the following calculation formulas:

$$\text{Encapsulation ratio} = \frac{\text{amount of Tac loaded in nanoparticles}}{\text{original feeding amount of Tac}} \times 100 = \frac{10.5}{12.5} \times 100 = 84\%$$

$$\text{Drug loading ratio} = \frac{\text{amount of Tac loaded in nanoparticles}}{\text{total amount of nanoparticles}} \times 100 = \frac{10.5}{135.5} \times 100 = 7.749\%.$$

The free radical scavenging testing

The DPPH (0.1 mM, 2 mL) ethanol solution was mixed with Tac@C-Mn_3O_4 (5 mg mL^{-1}), and an equal amount of water solution was added as a Control. The reaction mixture was shaken well and incubated at 37 °C in the dark for 30 minutes. A UV-2600 spectrophotometer (Shimadzu) was used for detection, with the scanning band set from 400 nm to 700 nm.

Cytotoxicity

HEK-293T cells were seeded at a density of 1×10^4 cells per well in 96-well plates and cultured overnight. The cytotoxic effects of Mn_3O_4, C-Mn_3O_4 and Tac@C-Mn_3O_4 at different concentrations were evaluated using the CCK-8 assay kit. HEK-293T cells (5×10^4 cells per well) were seeded onto 24-well plates and co-incubated with 50 μg mL^{-1} nanopreparation. Additionally, the cells were stained with Calcein-AM/PI and observed under a confocal laser scanning microscope (CLSM, TCS SP8) for live/dead cell staining assays.

Cellular uptake

HEK-293T cells were seeded at 1×10^5 cells per well in 24-well plates and incubated overnight. The cells were then treated with 50 μg mL^{-1} of CY5 (red fluorescence)-labeled C-Mn_3O_4 and Tac@C-Mn_3O_4 preparations and incubated for 1, 2, 4 and 8 h. Afterwards, they were incubated in 5 μg mL^{-1} DAPI (blue fluorescence) in serum-free medium for 15 minutes in the dark, washed with PBS, and analyzed under a CLSM using a 20× objective. The fluorescence intensity within the channel was quantified using a FACSCanto II flow cytometer.

ROS content

HEK-293T cells were seeded at 5×10^5 cells per well in 6-well plates and subjected to different treatments. The blank group received no additional treatment, while other groups were exposed to 100 μM H_2O_2 for 30 minutes to simulate the activated inflammatory microenvironment. Post-treatment, the cells were incubated with 50 μg mL^{-1} Mn_3O_4, C-Mn_3O_4, and Tac@C-Mn_3O_4 for 24 h. DCFH-DA solution was diluted 1 : 1000 with serum-free culture medium to a final concentration of 10 μmol L^{-1}, added to the cells, and incubated for 20 minutes at 37 °C. The cells were then washed three times with serum-free medium, collected and analyzed by flow cytometry.

Acute toxicity of Tac@C-Mn_3O_4

SD rats (6–8 weeks, male) were randomly divided into two groups, namely the PBS group and the Tac@C-Mn_3O_4 group (of different doses; n = 4), and the rats were injected through their tail vein. After 24 h of administration, the survival of the rats was recorded. 1.25% tribromoethanol was used for intraperitoneal anesthesia, and the rats were euthanized by cervical dislocation. The appearance of organs and pathological sections (H&E), as well as biochemical indicators of liver and renal function, was observed.

Biodistribution and targeting of Tac@C-Mn_3O_4

Fluorescence imaging was conducted using a small animal optical molecular *in vivo* imaging system (IVIS Spectrum; IVIS, Wahoo, MA, USA) equipped with appropriate optical filters. Doxorubicin (DOX) was administered on days 14 (4 mg kg^{-1}) and 7 (2 mg kg^{-1}) as part of the CKD model establishment. Parameters such as body weight, feeding, and water intake of the rats were monitored. The rats were categorized into four groups: the PBS, ICG, C-Mn_3O_4, and Tac@C-Mn_3O_4 groups. The initial treatment with nanopreparations was administered *via* tail vein injection on day 0 with doses of 14.97 mg kg^{-1} for Tac@C-Mn_3O_4 and 14.49 mg kg^{-1} for C-Mn_3O_4; the ICG and PBS groups received equivalent doses of pure ICG and PBS, respectively. Imaging was performed with the IVIS Lumina II at 1, 3, 6, 12, and 24 h post-injection. The exposure time was 5 seconds with an excitation wavelength of 640 nm. Post-euthanasia, organs such as the heart, liver, spleen, lungs, and kidneys were harvested for imaging to assess biodistribution and targeting capabilities *via* fluorescence intensity. All animal handling procedures were conducted in strict compliance with the guidelines approved by the Animal Ethics Committee (Institutional Animal Care and Use Committee of Shenzhen University Medical School, approval no. IACUC-202400030).

Tac@C-Mn_3O_4 *in vivo* treatment and biochemical analysis

Thirty SD rats with DOX-induced CKD were prepared as previously described and randomly divided into 6 groups, namely Blank (healthy rats, receiving equal amounts of saline), PBS (after model establishment, receiving equal amounts of saline), Tac (1.25 mg per kg per 2 days), Mn_3O_4 (14.49 mg per kg per 2 days), C-Mn_3O_4 (14.49 mg per kg per 2 days), and Tac@C-Mn_3O_4 (14.97 mg per kg per 2 days). At the end of the observation period, the rats were sacrificed, and serum and organ tissues were collected for biochemical analysis, including measurements of protein, urea nitrogen, creatinine, and inflammatory markers using standard commercial kits and histological staining procedures. The IL-1β, TNF-α, and ROS contents were measured in rat kidneys using the ELISA kit. Kidneys staining was collected and analyzed using H&E and PAS standard procedures.

Statistical analysis

Data were analyzed using GraphPad Prism 8 software (GraphPad Software, San Diego, CA, USA). Statistical significance was assessed using t-tests, with a p-value of less than 0.05 considered indicative of significant differences.

Results

Synthesis of nanopreparations

The formulation consists of Mn_3O_4, citric acid and Tac. Initially, an aqueous solution of $MnCl_2$ was dissolved in ethanolamine by a chemical synthesis process, followed by the preparation of Mn_3O_4 NPs *via* ultrasonication, centrifugation, washing and other operations. To enhance the performance of Mn_3O_4 NPs, citric acid was used to coat the nanoparticles, resulting in the production of citrate-modified C-Mn_3O_4 NPs.[16] The surface modification with the carboxyl-rich ligand trisodium citrate can significantly improve the stability and water solubility of Mn_3O_4 NPs, contributing to the negative surface charge and thereby enhancing their effectiveness and biocompatibility for future applications. Subsequently, the Tac drug was loaded onto the nanoparticles using a solvent evaporation technique. This method of drug loading facilitated a uniform distribution of Tac across the surface of C-Mn_3O_4 NPs, ensuring effective drug release and action. The synthetic yield of Mn_3O_4 was 18.06%. The encapsulation ratio was 84% and the loading ratio was 7.749%, as determined by UV adsorption spectroscopy. To aid in the visualization of the nanopreparations, the fluorescent dye indocyanine green (ICG) was loaded into C-Mn_3O_4 NPs under similar conditions. ICG, known for its robust fluorescence properties, allowed for clear observation under a fluorescence microscope. The integration of ICG with C-Mn_3O_4 NPs enabled the visual assessment of the distribution of C-Mn_3O_4 NPs, further confirming the feasibility and efficacy of the formulation.

Characterization of nanoparticles

According to the transmission electron microscopy (TEM) images shown in Fig. 1A, the Mn_3O_4 NPs displayed a spherical structure with a particle size ranging from 10 to 20 nm. Upon encapsulation with citric acid, both the dispersion and size of the NPs were significantly enhanced, reducing the particle size to 3–6 nm. Following the incorporation of Tac, the particle size of Tac@C-Mn_3O_4 increased, with sizes ranging from 6 to 20 nm, which further validated the successful loading. Additionally, after dye loading, the particle size of C-Mn_3O_4/ICG NPs was effectively maintained under 10 nm. To further confirm the successful preparation of Tac@C-Mn_3O_4 and characterize the nanopreparations, UV-vis and FT-IR absorption spectra analyses were performed. According to the UV-vis spectra shown in Fig. 1B, Mn_3O_4 exhibited a strong absorption peak in the visible region, consistent with its dark brown color. When modified by citric acid, the spectra of the modified nanoparticles overlapped with that of Mn_3O_4 in the infrared region, while significant changes were observed in the ultraviolet region, indicating successful citric acid functionalization. Upon loading Tac and ICG, their absorption bands at 600–800 nm overlapped, but their peaks exhibited a blueshift,

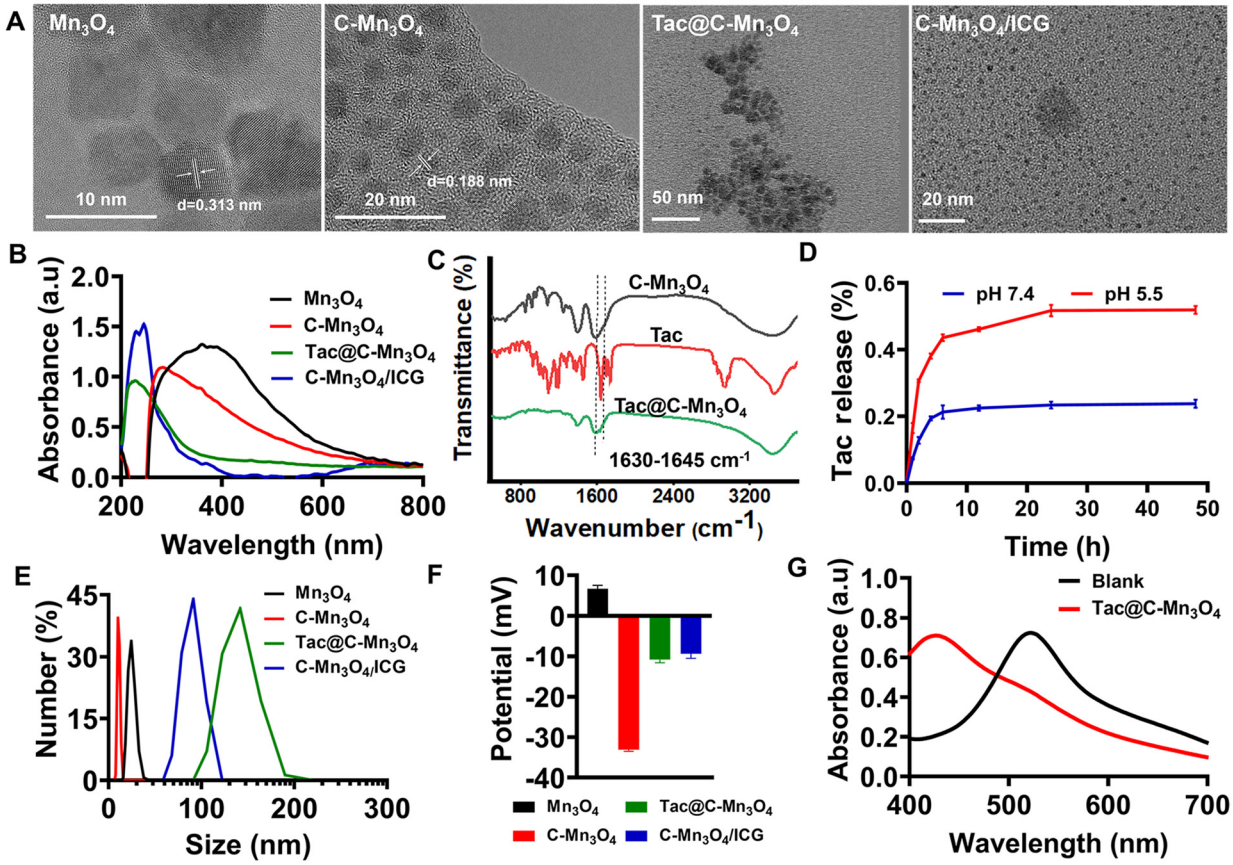

Fig. 1 (A) TEM images of Mn_3O_4, C-Mn_3O_4, Tac@C-Mn_3O_4, C-Mn_3O_4/ICG NPs, and their corresponding (B) UV absorption spectra. (C) FT-IR absorption spectra of C-Mn_3O_4, Tac, and Tac@C-Mn_3O_4. (D) Cumulative release of Tac from the C-Mn_3O_4@Tac NPs under different pH conditions *in vitro*. (E) Particle size distributions of Mn_3O_4, C-Mn_3O_4, Tac@C-Mn_3O_4, and C-Mn_3O_4/ICG NPs, along with their (F) zeta potentials. (G) Radical scavenging capacity of Tac@C-Mn_3O_4. Values are expressed as mean ± standard deviation (SD).

likely due to the interaction between the –COOH group of citric acid and the molecules of Tac and dye. FT-IR absorption spectra results, displayed in Fig. 1C, indicated that C-Mn_3O_4@Tac and C-Mn_3O_4 shared similar waveform and characteristic peaks. Furthermore, the C═O vibration peak characteristic of the Tac-specific amide bond was observed at 1630–1645 cm^{-1}, which was also observed on the Tac@C-Mn_3O_4, confirming the successful loading of Tac onto C-Mn_3O_4. The cumulative release results *in vitro* were shown in Fig. 1D, Tac@C-Mn_3O_4 exhibited the same release trend at pH 5.5 and pH 7.4, with gradual released in the first 6 h, reaching saturation at 24 h. The cumulative release rate at pH 5.5 was higher than that at pH 7.4, indicating that the release in the CKD kidney environment exceeded that in the normal physiological environment. The UV serum test results demonstrated that the intensity of the absorption peaks for Tac@C-Mn_3O_4 (297 nm) and C-Mn_3O_4/ICG (251 nm) remained stable over 72 h, without any significant shift, thus confirming the excellent chemical stability of the formulation (Fig. S1†). Finally, the detection of particle size and zeta potential in Fig. 1E further confirmed the impact of citric acid functionalization on the hydrated particle size of Mn_3O_4 NPs and revealed an increase in the hydrated particle size following drug or dye loading. Zeta potential measurements indicated that the potentials of Mn_3O_4, C-Mn_3O_4, Tac@C-Mn_3O_4, and C-Mn_3O_4/ICG were 6.66 ± 0.89 mV, −33.1 ± 0.4 mV, −10.8 ± 0.6 mV, and −9.34 ± 1.09 mV, respectively, suggesting good stability for these preparations, as shown in Fig. 1F. The excitation wavelength (Ex), emission wavelength (Em) and fluorescence imaging results after loading ICG are shown in Fig. S2.† When the ICG dye was loaded, it was quenched by C-Mn_3O_4. Considering that C-Mn_3O_4 had significant absorption characteristics in the range of 250–800 nm, it absorbed a certain amount of light, thereby causing quenching. Notably, the Ex of C-Mn_3O_4/ICG was red-shifted, suggesting that ICG was adsorbed on the surface of C-Mn_3O_4 and charged transfer occurred; or because the particle size of C-Mn_3O_4 was small, there was a quantum size effect that affects the excitation energy level of ICG.

ROS scavenging ability

Finally, the free radical scavenging capability of Tac@C-Mn_3O_4 was assessed using DPPH free radicals, with an equivalent volume of aqueous solution serving as a blank control. DPPH

was characterized by its dark purple color and a distinct absorption peak at 517 nm. In the presence of free radical scavengers, the single electrons of DPPH were captured, leading to a lighter hue and a reduction in absorbance values at this characteristic wavelength. As depicted in Fig. 1G, the maximum absorption peak at 517 nm nearly disappeared following the introduction of Tac@C-Mn_3O_4, and the recorded absorbance value was significantly reduced, demonstrating the compound's exceptional free radical scavenging effectiveness responsiveness. In conclusion, the ultra-small drug-loaded and dye-loaded formulations provided in this study exhibited remarkable stability and potential to specifically target the kidney with ROS scavenging capability, thereby providing crucial support for the establishment of a targeted nano-therapy platform for renal diseases.

Cytotoxicity

The Cell Counting Kit-8 (CCK-8) method was employed to assess the *in vitro* cytotoxicity of Mn_3O_4, C-Mn_3O_4, and Tac@C-Mn_3O_4 on human embryonic kidney cells (HEK-293T). As shown in Fig. 2A, the cytotoxicity of Mn_3O_4, C-Mn_3O_4 and Tac@C-Mn_3O_4 to HEK-293T cells was negligible at concentrations below 50 μg mL^{-1}, and no significant reduction in cell viability was observed. Upon increasing the concentration of the formulation, the nanopreparation exhibited varying degrees of cytotoxic effects on HEK-293T (Fig. 2B). At a concentration of 100 μg mL^{-1}, a marked difference in the cytotoxicity between C-Mn_3O_4 and Tac@C-Mn_3O_4 was noted, suggesting that the incorporation of Tac increased the cytotoxicity potential of the nanopreparation. When the concentration of the nanopreparation exceeded 100 μg mL^{-1}, the viability of HEK-293T cells progressively declined as the concentration increased. Consequently, to mitigate the adverse effects of high drug concentrations on normal tissues, the concentration of therapeutic agents should be maintained below 100 μg mL^{-1} to enhance biosafety.

Live/dead cell staining experiment

In addition, the toxicity of nanopreparations at 50 μg mL^{-1} HEK-293T cells was further evaluated through live/dead cell staining experiments. As shown in Fig. 2C, there was no significant difference in cell viability between the groups treated with Mn_3O_4, C-Mn_3O_4, and Tac@C-Mn_3O_4 compared to the control group, and extensive green fluorescence (indicative of

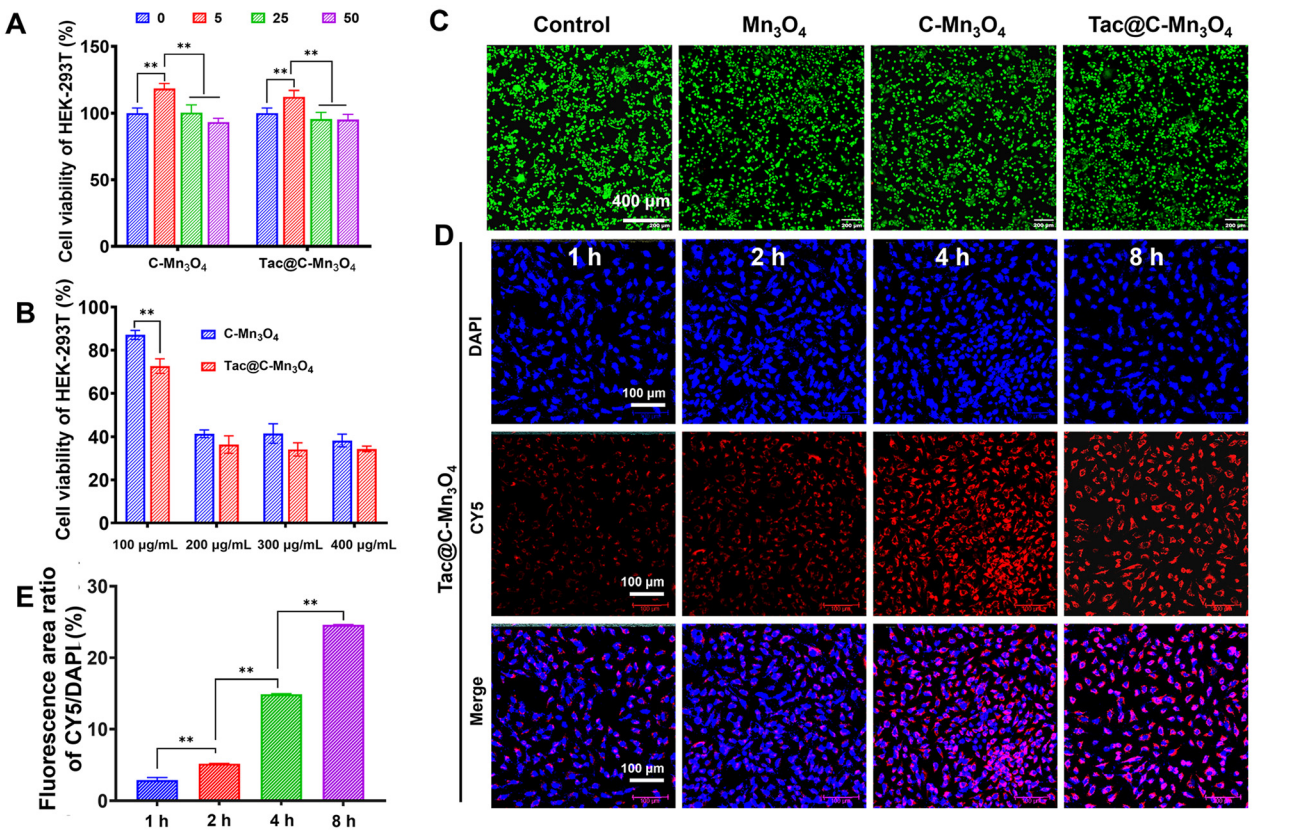

Fig. 2 (A and B) Cell viability of HEK-293T cells was assessed using different nanopreparations and concentrations by CCK-8 assay. (C) Fluorescence microscopy images of Mn_3O_4, C-Mn_3O_4, and Tac@C-Mn_3O_4 of live/dead cells stained with HEK-293T cell survival. (D) Fluorescence CLSM images of HEK-293T cells stained with DAPI and CY5 to evaluate the cell uptake of Tac@C-Mn_3O_4. (E) Quantification of fluorescence for the cellular uptake of Tac@C-Mn_3O_4. *p < 0.05, **p < 0.01, ***p < 0.001, and ****p < 0.0001, where ns indicates no significance. Values are expressed as mean ± SD (n = 3).

viable cells) was observed in the microscope images. This result confirmed that 50 μg mL^{-1} was a safe concentration for nanopreparations, and is suitable for use in subsequent *in vitro* and *in vivo* applications.

Cell uptake

Considering the critical role of nanopreparation internalization for effective drug delivery, colocalization analysis using confocal laser scanning microscopy (CLSM) images was employed to evaluate cell uptake at different incubation times (1 h, 2 h, 4 h, 8 h). The nuclei of HEK-293T cells were stained with DAPI dye, which emitted blue fluorescence, while C-Mn_3O_4 and Tac@C-Mn_3O_4 were labeled with Cy5, emitting red fluorescence. As the incubation time increased, the intensity of red fluorescence from CY5 bound to the nanopreparation also increased (Fig. 2D and Fig. S3†). Notably, after a brief incubation for 4 h, a significant amount of nanopreparations was internalized into HEK-293T cells, and the images exhibited high degrees of colocalization. The enhanced cell uptake capacity was more clearly observed through quantitative analysis of fluorescence images (Fig. 2E and Fig. S4†). These experimental results showed that HEK-293T cells possess a high capacity for taking up C-Mn_3O_4 and Tac@C-Mn_3O_4, with the rate of intake showing a consistent upward trend over time. This provides a vital experimental foundation for the targeted transport of functional molecules to lesion sites, serving as a robust drug delivery system for nanopreparations.

Tac@C-Mn_3O_4 induced mitochondrial damage

The integrity of mitochondria in response to different nanopreparations was observed by JC-1 staining. In this technique, the green JC-1 monomer indicates the depolarized membrane mitochondria, whereas the red JC-1 aggregate reflects mitochondria with normal membrane potential. As shown in Fig. 3A, the red fluorescence within the cells was significantly diminished under a simulated inflammatory microenvironment (H_2O_2 treatment), signifying substantial mitochondrial structural damage. Concurrently, there was a reduction in mitochondrial membrane potential, suggesting a potential inclination towards early apoptosis. It is particularly significant that the ratio of red/green fluorescence of membrane potential was markedly higher following the Tac@C-Mn_3O_4 treatment compared to the H_2O_2 treatment alone (Fig. 3B). The findings from flow cytometry analysis were in alignment with those from the mitochondrial membrane potential staining experiments.

ROS scavenging capability

H_2O_2 exposure induced an increase in ROS content in HEK-293T cells, while intervention with Mn_3O_4, C-Mn_3O_4, and

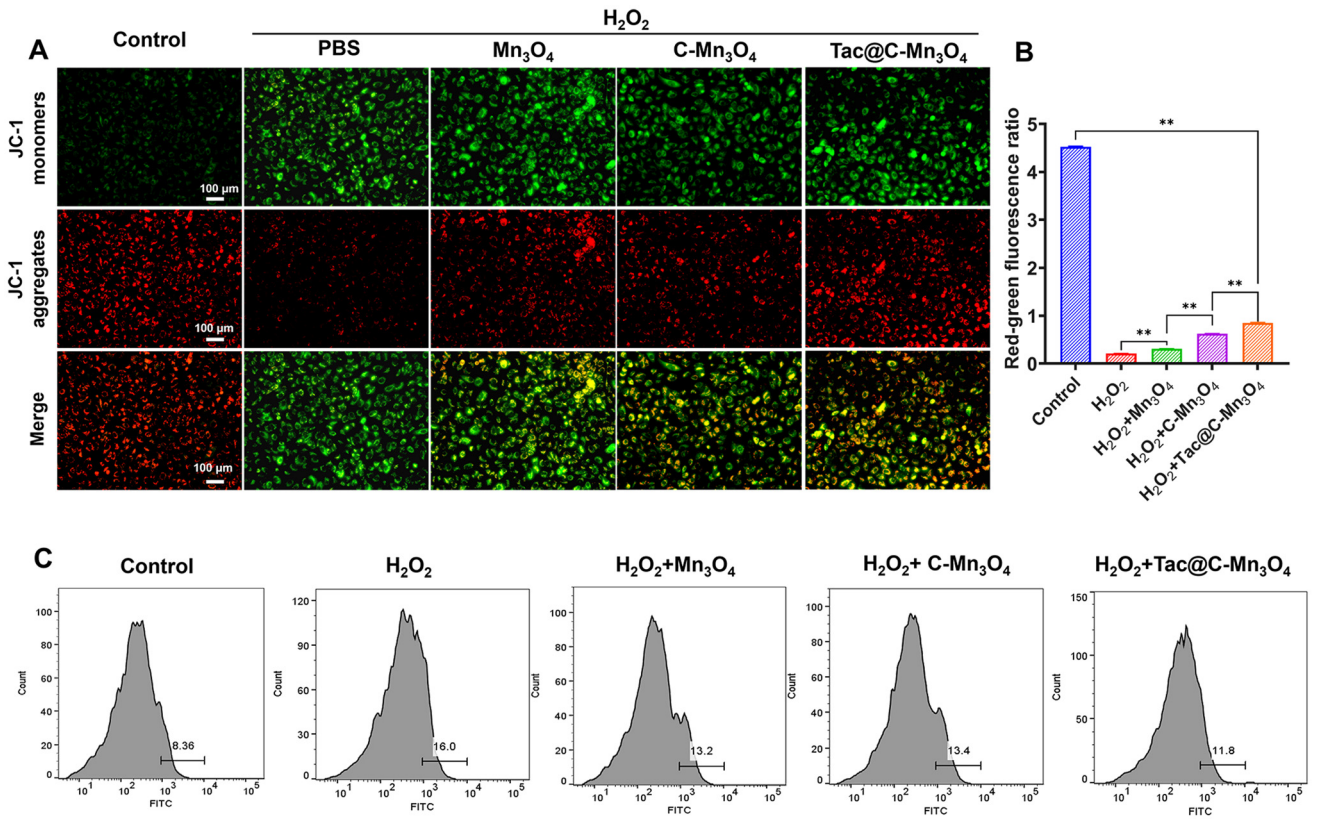

Fig. 3 (A) CLSM images of HEK-293T cells stained with JC-1 (20×) to evaluate the effects of Mn_3O_4, C-Mn_3O_4, and Tac@C-Mn_3O_4 on mitochondrial membrane potential under H_2O_2 treatment, along with their (B) fluorescence quantification analysis. (C) The ROS in HEK-293T cells after H_2O_2 treatment with Mn_3O_4, C-Mn_3O_4, and Tac@C-Mn_3O_4 were analyzed by flow cytometry. Statistical significance was denoted as follows: *p < 0.05, **p < 0.01, ***p < 0.001, and ****p < 0.0001, where ns indicates no significance. Values are expressed as mean ± SD (n = 3).

Tac@C-Mn_3O_4 resulted in a significant decrease in ROS levels compared to the H_2O_2-treated group, as illustrated in Fig. 3C. The experimental results demonstrated that Tac@C-Mn_3O_4 effectively contributed to maintaining cellular redox homeostasis, positioning it as a potential therapeutic agent for *in vivo* applications.

Acute toxicity of Tac@C-Mn_3O_4 *in vivo*

To evaluate the acute toxicity of Tac@C-Mn_3O_4 *in vivo*, SD rats were divided into two groups: the PBS group and the Tac@C-Mn_3O_4 treatment group of various concentrations. The survival of the rats, H&E staining of the main organs, and serum biochemical indicators were observed after tail vein injection of the drug. All rats died 24 h after the injection of 500 mg kg^{-1} Tac@C-Mn_3O_4 (Table S1†). The appearance of the isolated organs showed that the lungs of rats injected with 250 mg kg^{-1} Tac@C-Mn_3O_4 underwent organ changes (Fig. S5A†). The organs were then stained with H&E. The results showed that rats injected with 250 mg kg^{-1} Tac@C-Mn_3O_4 exhibited significant damage to the liver, lungs, and kidneys; while those injected with 125 mg kg^{-1} Tac@C-Mn_3O_4 showed slight damage to these organs; the other doses did not cause obvious damage compared with the PBS group (Fig. S5B†). Serum was collected for blood biochemistry, and liver and kidney function indexes of rats were detected. The results are shown in Fig. S6.† Among them, the liver function index AST of Tac@C-Mn_3O_4 injected at concentrations of 125 mg kg^{-1} and 250 mg kg^{-1} exceeded the normal range, and the kidney function index Ca was lower than the normal range; the liver function indexes ALT, ALP, Glu, and TP and the kidney function indexes creatinine and blood urea nitrogen (BUN) of the other doses were all within the normal range, indicating that high doses caused liver and kidney damage. This indicated that Tac@C-Mn_3O_4 at concentrations below 62.5 mg kg^{-1} was considered safe for further experimental use.

In vivo metabolism and therapeutic potential of Tac@C-Mn_3O_4

To evaluate the potential of Tac@C-Mn_3O_4 for treating CKD *in vivo*, rats were randomly assigned to four groups: Control (PBS), ICG, C-Mn_3O_4/ICG (C-Mn_3O_4) and Tac@C-Mn_3O_4/ICG (Tac@C-Mn_3O_4). Treatment was administered *via* tail vein injection. The rats were subsequently imaged using the IVIS Lumina II system, and their major organs were collected for *ex vivo* fluorescence imaging post-treatment. As shown in Fig. 4A, following administration of the nanopreparation, the

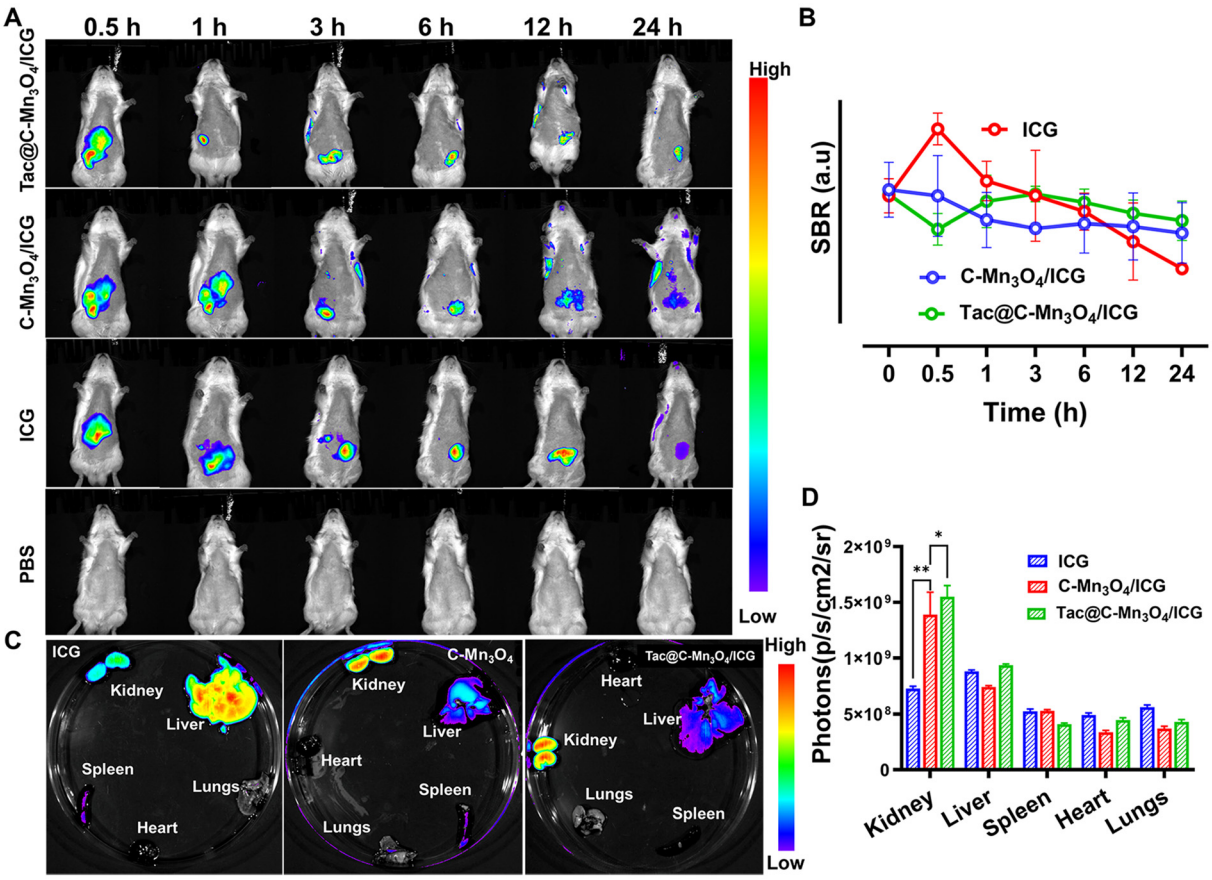

Fig. 4 (A) Representative *in vivo* biofluorescence images of the model rat metabolism within 24 h after PBS, ICG, C-Mn_3O_4/ICG and Tac@C-Mn_3O_4/ICG treatments. (B) Quantification of the signal-to-background ratios (SBRs) for the images in (A). (C) *Ex vivo* fluorescence images of the main organs from euthanized rats, and their (D) fluorescence quantification analysis. Statistical significance was denoted as follows: *$p < 0.05$, **$p < 0.01$, ***$p < 0.001$, and ****$p < 0.0001$, where ns indicates no significance. Values are expressed as mean ± SD ($n = 3$).

ICG group exhibited a more concentrated fluorescence and high intensity at 3–12 h. This fluorescence diminished following metabolic processes in the liver, kidneys, and intestines, showing a marked decrease at 24 h. In contrast, the C-Mn_3O_4/ICG group and the Tac@C-Mn_3O_4/ICG group demonstrated enhanced accumulation of the nanopreparation. Post-metabolic processing *in vivo* resulted in significant retention of fluorescence in the renal area, which remained pronounced even after 24 h. Twenty-four hours post-injection, the organs of each group of rats (including the heart, liver, spleen, lung, and kidneys) were excised for *in vitro* imaging, with results aligning closely with those observed *in vivo* (Fig. 4B). Notably, in both the C-Mn_3O_4/ICG and Tac@C-Mn_3O_4/ICG groups, nanopreparations were substantially enriched in the kidney. Further qualification of fluorescence intensity across the groups revealed that the nanopreparation not only predominantly localized to the liver and kidneys but also exhibited significantly higher intensity compared to the ICG group (Fig. 4C). These findings suggest that ultra-small Tac@C-Mn_3O_4/ICG particles were effectively targeted and accumulated in the kidneys, avoiding rapid excretion. The gradual degradation of the nanopreparation and the sustained release of the drug further suppressed renal excretion, highlighting the potential for effective CKD treatment.

Tac@C-Mn_3O_4 treatment of CKD rats *in vivo*

In the forthcoming study, a DOX-induced model of CKD rats will be established to further assess the therapeutic effect of the nanopreparation *in vivo*. Renal injury was induced in rats through two tail vein injections of DOX. Experimental procedures will commence seven days following the second DOX injection, with equal doses of PBS, Tac, Mn_3O_4, C-Mn_3O_4 and Tac@C-Mn_3O_4 administered bi-daily (Fig. 5A). The food and water intakes of the rats in each group were monitored within 24 h post-model induction, and the data are presented in Table S2†. Relative to normal rats (Blank), CKD rats treated solely with PBS exhibited symptoms such as increased water intake, reduced food intake, and weight loss. Following the treatment with nanopreparations, significant improvements were observed in both the food and water intakes of the CKD rats. Over the 28 days of treatment, there was no notable difference in body weight between the C-Mn_3O_4 and Tac@C-Mn_3O_4 groups compared to the Blank group (Fig. 5B). Additionally, the renal index of rats was evaluated. As illustrated in Fig. 5C, the renal index of rats in the PBS-treated group significantly increased post-treatment, approximately 2.6 times higher than that of the Tac@C-Mn_3O_4 treatment group. Post-treatment with Tac@C-Mn_3O_4, the renal index significantly decreased, aligning closely with the values seen in the Blank group and slightly lower than those observed in the Tac treatment group.

Anti-inflammatory and antioxidant capacities of Tac@C-Mn_3O_4

Albuminuria, proteinuria and hypoalbuminemia, which are hallmark clinical indicators of CKD, were utilized to monitor glomerular filtration status and disease progression. As depicted in Fig. 5D–F, serum albumin (SAlb) levels decreased in the PBS-treated group compared to the Blank group, whereas urine albumin (UAlb) and total protein (UTP) levels increased, aligning with symptoms indicative of kidney injury and impaired glomerular and tubular filtration. However, these parameters were significantly ameliorated following the treatment with Tac@C-Mn_3O_4 NPs and Tac. BUN and serum creatinine (Scr) levels, crucial for evaluating renal function,[25] are shown in Fig. 5G and H. In the PBS group, elevated serum BUN and Scr levels were observed, reflecting their accumulation due to kidney damage. Notably, in the Tac@C-Mn_3O_4 treated group, BUN levels reduced from 2.59 ± 0.22 mg mL^{-1} to 0.33 ± 0.01 mg mL^{-1}, and Scr levels decreased from 0.35 ± 0.08 μmol mL^{-1} to 0.14 ± 0.04 μmol mL^{-1}. These findings indicate that the treatment mitigated proteinuria and slowed CKD progression, potentially enhancing disease management.

Macrophage infiltration in the kidneys and the subsequent rise in pro-inflammatory cytokines (*e.g.*, TNF-α, IL-1β, *etc.*) were critical aspects of CKD.[26–28] Accordingly, the levels of inflammatory mediators and ROS in the kidneys were measured, as shown in Fig. 5J–L. Compared to the Blank group, the PBS group exhibited elevated TNF-α, IL-1β, and ROS levels, confirming kidneys damage and successful establishment of the CKD model. Post-treatment improvements were significant, with statistical analysis demonstrating notable reductions in inflammatory markers and ROS, attributed to the effective modulation of inflammatory and oxidative stress pathways by Tac@C-Mn_3O_4 NPs.

Histopathological studies

The hematoxylin and eosin (H&E) staining test was employed to observe the pathological changes of kidney sections under various treatment conditions. In the Blank group, the renal tubules were neatly arranged, and the glomeruli were well-formed and regular, consistent with typical renal structural characteristics. Conversely, in CKD rats treated with PBS, the renal tubules appeared dilated and the normal morphology of the glomeruli was disrupted. In contrast, the extent of focal tubular dilation and glomerular necrosis was significantly reduced after treatment with Tac@C-Mn_3O_4 NPs, indicating that nano-therapy exerted a considerable protective effect on DOX-induced kidney injury.

To evaluate whether Tac@C-Mn_3O_4 treatment could mitigate glomerulosclerosis in CKD rats, PAS staining was performed on kidney sections. The sections from the model group exhibited significant kidney damage, characterized by damaged glomerular structures, glycogen accumulation, and tubular dilation. The treatment groups receiving Mn_3O_4, Tac, and C-Mn_3O_4 displayed varying degrees of glomerulosclerosis. However, the Tac@C-Mn_3O_4 treatment group demonstrated uniform glomerular integrity and even glycogen distribution in the interstitial cells, mirroring the characteristics observed in the control group. This indicates that Tac@C-Mn_3O_4 treatment could potentially alleviate glomerulosclerosis in CKD rats. Overall, these findings suggest that Tac@C-Mn_3O_4 nanoparticles effectively restore significant pathological changes in

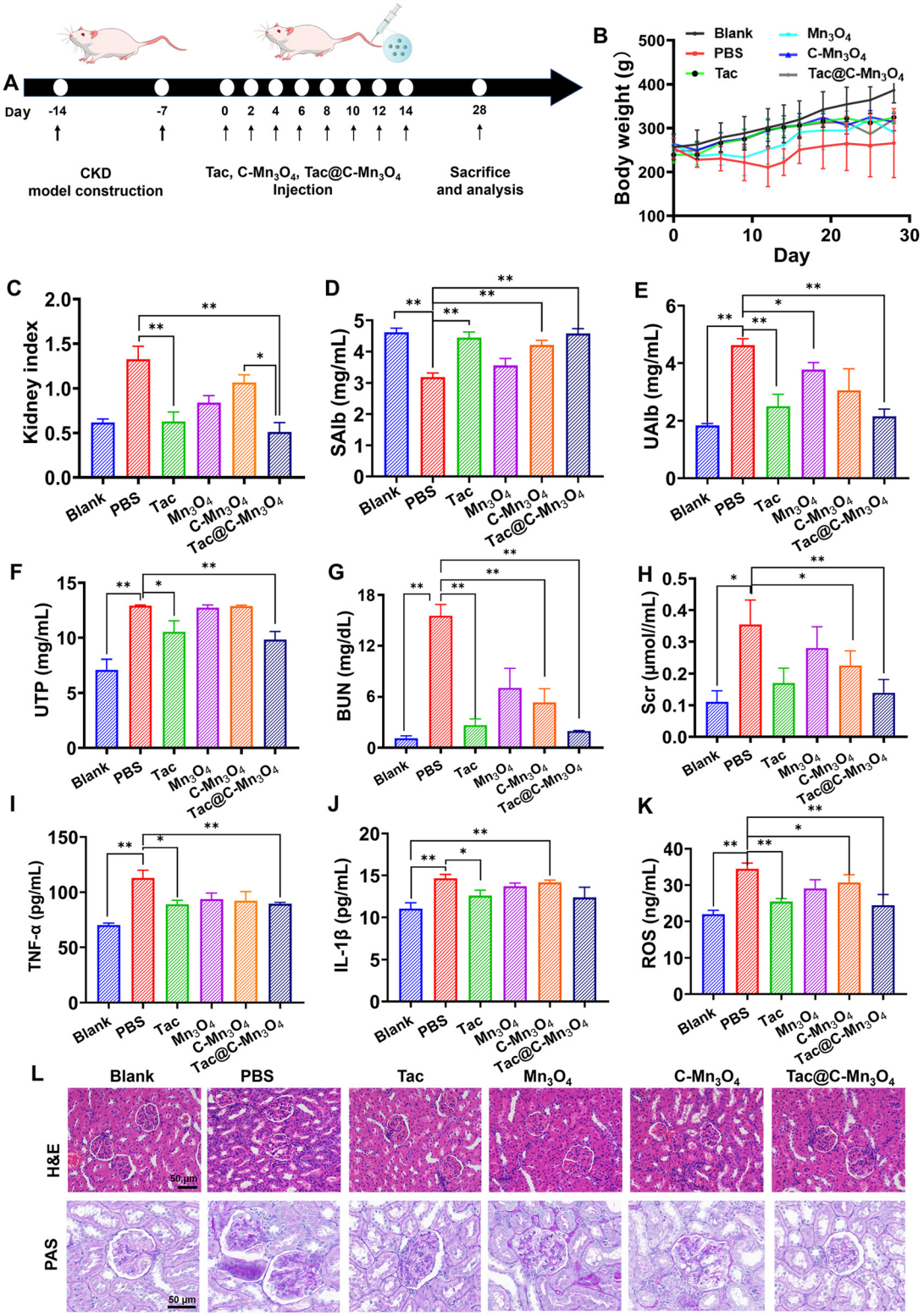

Fig. 5 (A) Schematic diagram of the specific *in vivo* study protocol. (B) Body weight of rats in each group at the end of the trial period, and their corresponding (C) renal index. (D and E) Serum albumin (SAlb) and urine albumin (UAlb) content. (F) Urine total protein (UTP) content. (G and H) Blood urea nitrogen (BUN) and serum creatinine (Scr) content. (I and J) Expression of inflammatory factors (TNF-α and IL-1β) and their (K) ROS content in rat kidneys after treatment with each group of nanopreparations. (L) Representative images of H&E staining and PAS staining in rat kidneys (200× and 400×, respectively). Statistical significance was denoted as follows: $*p < 0.05$, $**p < 0.01$, $***p < 0.001$, and $****p < 0.0001$, where ns indicates no significance. Values are expressed as mean ± SD ($n = 3$).

the kidney structure in CKD models, providing strong support for their potential as a therapeutic tool.

Discussion

Patients with CKD often exhibit clinical symptoms such as reduced nephron numbers, glomerulosclerosis, and arteriosclerosis, which may culminate in life-threatening renal failure.[25] As a complex and essential organ, the kidney presents significant challenges in achieving targeted organ/cellular delivery with conventional therapeutic drugs. Consequently, the development of specialized drug delivery systems for the kidney represents a crucial and emerging direction in the treatment of CKD. Nanomaterials, recognized for their superior drug distribution and therapeutic potential, particularly through engineering modifications that enhance kidney targeting, offer considerable hope for CKD management.[26] Nonetheless, the unique structural characteristics of the kidney and the glomerular filtration barrier impose stringent requirements on the particle size, charge, and structural rigidity of NPs, necessitating further advancements in carrier suitability and targeting efficiency.[27]

In this study, we developed ultra-small nanopreparations (Tac@C-Mn_3O_4 NPs), which incorporate citrate, Mn_3O_4, and the immunosuppressant Tac, achieving passive accumulation and sustained drug release in the presence of enhanced EPR by targeting the inflammatory microenvironment. Tac@C-Mn_3O_4 NPs have been identified as an effective treatment for antioxidative stress and anti-inflammatory synergistic treatment of CKD, addressing both the high incidence of CKD and the shortage of effective therapeutic options in the medical field.

The kidney, a critical organ for bodily functions, is rich in mitochondrial structures that play pivotal roles in various molecular pathways, including macromolecular synthesis, maintenance of cellular redox balance, and regulation of inflammation and cell death.[28,29] Excessively produced ROS in mitochondria serve as auxiliary messengers in cell signaling, influencing key processes such as metabolic cell survival and death.[30] Previous studies have shown that ROS accumulation is closely associated with CKD pathogenesis.[31] The imbalance in oxidative stress and inflammation induced by persistently high levels of ROS can severely compromise cellular structure and function leading to cell death.

Our study indicated that Mn_3O_4 NPs, by mimicking enzymatic activities, effectively maintain cellular redox balance by scavenging ROS and concurrently inhibit the onset of inflammatory responses, enhanced by the immunosuppressant Tac. This mechanism underscores a significant role of the ROS-mediated redox and anti-inflammatory pathways in protecting kidney function. The capability of Tac@C-Mn_3O_4 NPs to protect the structural and functional integrity of mitochondria, mitigate oxidative damage, remove excess ROS to preserve cellular redox balance, and suppress the expression of pro-inflammatory cytokines has been corroborated through cell and animal studies. These interventions allow the normalization of crucial CKD markers such as Salb, UTP, and BUN, indicating a promising two-pronged strategy for CKD treatment. Collectively, these results provide preliminary evidence that redox-based nanopreparations represent a novel approach for addressing CKD through anti-oxidative stress and anti-inflammatory pathways, showcasing significant potential for clinical application.

Conclusions

In this study, we report a novel Mn_3O_4-based bifunctional ultra-small nanopreparation, Tac@C-Mn_3O_4, designed for effective CKD treatment. The surface of Mn_3O_4 NPs was functionalized with citric acid, followed by the loading of the drug tacrolimus, enhancing water solubility, biosafety, and therapeutic potential. This ultra-small nanopreparation, with a size of less than 10 nm and an electronegative surface, demonstrated the potential for renal system accumulation and sustained drug release. Tac@C-Mn_3O_4 demonstrated enhanced anti-inflammatory and oxidative stress regulatory effects compared to those of the single-agent Tac or C-Mn_3O_4 NPs alone. *In vitro* and *in vivo* experiments indicate that Tac@C-Mn_3O_4 could rapidly and specifically accumulate in the injured kidney, improve the renal function, reduce inflammation levels, and alleviate the pathological changes in kidney tissue of CKD-afflicted rats. In summary, this innovative ultra-small nanopreparation showed potent kidney-targeting capabilities in treating CKD by combining anti-inflammatory actions and scavenging excess ROS to regulate oxidative stress, potentially offering new perspectives and breakthroughs in the treatment of kidney diseases.

Ethics approval and consent to participate

All animal handling procedures were performed in accordance with the guidelines approved by the Animal Ethics Committee (Institutional Animal Care and Use Committee of Shenzhen University Medical School, approval no. IACUC-202400030).

Author contributions

Qin Wang: conceptualization, investigation, data curation, software, formal analysis, methodology, visualization, writing – original draft, writing – review & editing, resources, visualization, funding acquisition, and project administration. Xuedan Nie: conceptualization, investigation, data curation, software, formal analysis, methodology, visualization, writing – original draft, and writing – review & editing. Wenting Shang: conceptualization, investigation, data curation, software, formal analysis, methodology, visualization, writing – original draft, writing – review & editing, resources, visualization, and project

administration. Haiyan Qiu: data curation, software, formal analysis, methodology, visualization, writing – original draft, and writing – review & editing. Yeping Ren: conceptualization, investigation, data curation, software, formal analysis, methodology, visualization, writing – original draft, and writing – review & editing. Yifan Song, Liting Chen, He Zhu, Xueli Zhang, Mengru Yang, Xiaohui Xu, Peidan Chen, Chao Zhang, and Jia Xu: investigation, data curation, software, formal analysis, methodology, and writing – review & editing.

Data availability

The authors declare that all data supporting the results in this study are available within the paper and its additional file.

Conflicts of interest

The authors declare that they have no known competing financial interests or personal relationships that could have appeared to influence the work reported in this paper.

Acknowledgements

This study was supported by the National Natural Science Foundation of China (82270774, 81900649), the Beijing Municipal Natural Science Foundation (7242276), and the Science Technology and Innovation Committee of Shenzhen Municipality (JCYJ20210324094804013).

References

1 V. Jha, G. Garcia-Garcia, K. Iseki, Z. Li, S. Naicker, B. Plattner, R. Saran, A. Y.-M. Wang and C.-W. Yang, *Lancet*, 2013, **382**, 260–272.
2 K. Kalantar-Zadeh, T. H. Jafar, D. Nitsch, B. L. Neuen and V. Perkovic, *Lancet*, 2021, **398**, 786–802.
3 A. Shrestha and R.-C. Che, *Adv. Exp. Med. Biol.*, 2019, **1165**, 325–346.
4 G. R. Matzke, G. R. Aronoff, A. J. Atkinson, Jr., W. M. Bennett, B. S. Decker, K.-U. Eckardt, T. Golper, D. W. Grabe, B. Kasiske, F. Keller, J. T. Kielstein, R. Mehta, B. A. Mueller, D. A. Pasko, F. Schaefer, D. A. Sica, L. A. Inker, J. G. Umans and P. Murray, *Kidney Int.*, 2011, **80**, 1122–1137.
5 J. Jamaluddin, M.-S. Mohamed-Yassin, S. N. Jamil, M. A. M. Kamel and M. Y. Yusof, *Heliyon*, 2023, **9**, e14998.
6 G. Keller, G. Zimmer, G. Mall, E. Ritz and K. Amann, *N. Engl. J. Med.*, 2003, **348**, 101–108.
7 H. Peng, F. Yao, J. Zhao, W. Zhang, L. Chen, X. Wang, P. Yang, J. Tang and Y. Chi, *Exploration*, 2023, **3**, 20220115.
8 M. H. Elbatreek, M. P. Pachado, A. Cuadrado, K. Jandeleit-Dahm and H. H. H. W. Schmidt, *Trends Endocrinol. Metab.*, 2019, **30**, 312–327.
9 S. Kishi, H. Nagasu, K. Kidokoro and N. Kashihara, *Nat. Rev. Nephrol.*, 2024, **20**, 101–119.
10 Q. Wu, L. Yang, L. Zou, W. Yang, Q. Liu, A. Zhang, J. Cao, G. Shi, J. He and X. Yang, *Adv. Healthcare Mater.*, 2023, **12**, e2300632.
11 K. A. Mapuskar, G. Vasquez-Martinez, G. Mayoral-Andrade, A. Tomanek-Chalkley, D. Zepeda-Orozco and B. G. Allen, *Biomedicines*, 2023, **11**, 1573.
12 L. Wang, B. Zhu, Y. Deng, T. Li, Q. Tian, Z. Yuan, L. Ma, C. Cheng, Q. Guo and L. Qiu, *Adv. Funct. Mater.*, 2021, **31**, 2101804.
13 R. Yuan, Y. Li, S. Han, X. Chen, J. Chen, J. He, H. Gao, Y. Yang, S. Yang and Y. Yang, *ACS Cent. Sci.*, 2022, **8**, 10–21.
14 E. Niki, *Arch. Biochem. Biophys.*, 2016, **595**, 19–24.
15 H. H. H. W. Schmidt, R. Stocker, C. Vollbracht, G. Paulsen, D. Riley, A. Daiber and A. Cuadrado, *Antioxid. Redox Signaling*, 2015, **23**, 1130–1143.
16 A. Adhikari, S. Mondal, T. Chatterjee, M. Das, P. Biswas, R. Ghosh, S. Darbar, H. Alessa, J. T. Althakafy, A. Sayqal, S. A. Ahmed, A. K. Das, M. Bhattacharyya and S. K. Pal, *Commun. Biol.*, 2021, **4**, 1013.
17 Y. Ma, F. Cai, Y. Li, J. Chen, F. Han and W. Lin, *Bioact. Mater.*, 2020, **5**, 732–743.
18 H.-T. Cheng, H.-C. Huang, T.-Y. Lee, Y.-H. Liao, Y.-H. Sheng, P.-R. Jin, K.-W. Huang, L.-H. Chen, Y.-T. Chen, Z.-Y. Liu, T.-C. Lin, H.-C. Wang, C.-H. Chao, I. P. Juang, C.-T. Su, K.-H. Huang, S.-L. Lin, J. Wang, Y.-C. Sung and Y. Chen, *J. Controlled Release*, 2022, **346**, 169–179.
19 Z. Chen, H. Peng and C. Zhang, *Int. J. Pharm.*, 2020, **587**, 119679.
20 L. Li, J. Guo, Y. Wang, X. Xiong, H. Tao, J. Li, Y. Jia, H. Hu and J. Zhang, A Broad-Spectrum ROS-Eliminating Material for Prevention of Inflammation and Drug-Induced Organ Toxicity, *Adv. Sci.*, 2018, **5**, 1800781.
21 P. Wu, M. Gao, C. Zhang, C. Li, G. Li, X. Yan, X. Lai, Y. Zhang and J. Zhang, *Adv. Funct. Mater.*, 2022, **32**, 2205528.
22 J. Yang, R. Zhang, H. Zhao, H. Qi, J. Li, J. F. Li, X. Zhou, A. Wang, K. Fan, X. Yan and T. Zhang, *Exploration*, 2022, **2**, 20210267.
23 J. Yao, Y. Cheng, M. Zhou, S. Zhao, S. Lin, X. Wang, J. Wu, S. Li and H. Wei, *Chem. Sci.*, 2018, **9**, 2927–2933.
24 J. Shen, C. Liu, P. P. Yan, M. F. Wang, L. Y. Guo, S. H. Liu, J. H. Chen, J. M. Rosenholm, H. F. Huang, R. D. Wang and H. B. Zhang, *Research*, 2022, **2022**, 9794235.
25 G. R. Saranya and P. Viswanathan, *Biomed. Pharmacother.*, 2023, **161**, 114447.
26 R. L. Amdur, H. I. Feldman, J. Gupta, W. Yang, P. Kanetsky, M. Shlipak, M. Rahman, J. P. Lash, R. R. Townsend, A. Ojo, A. Roy-Chaudhury, A. S. Go, M. Joffe, J. He, V. S. Balakrishnan, P. L. Kimmel, J. W. Kusek, D. S. Raj and C. S. Investigators, *Clin. J. Am. Soc. Nephrol.*, 2016, **11**, 1546–1556.
27 H. W. Kim, C. K. Lee, H. S. Cha, J. Y. Choe, E. J. Park and J. Kim, *Rheumatol. Int.*, 2015, **35**, 727–734.

28 B. T. Lee, F. A. Ahmed, L. L. Hamm, F. J. Teran, C. S. Chen, Y. X. Liu, K. Shah, N. Rifai, V. Batuman, E. E. Simon, J. He and J. Chen, *BMC Nephrol.*, 2015, **16**, 77.
29 T. K. Chen, M. P. Hoenig, D. Nitsch and M. E. Grams, *Br. Med. J.*, 2023, **383**, e074216.
30 N. Trac, A. Ashraf, J. Giblin, S. Prakash, S. Mitragotri and E. J. Chung, *ACS Nano*, 2023, **17**, 6165–6177.
31 Y. Huang, J. Wang, K. Jiang and E. J. Chung, *J. Controlled Release*, 2021, **334**, 127–137.